

1 Assessment of the impact of CO₂ storage in sandstone for-
2 mations by experimental studies and geochemical modeling:
3 the case of the Mesohellenic Trough, NW Greece

4
5 **Koukouzas Nikolaos^a, Kypridou Zacharenia^b, Purser Gemma^c, Rochelle**
6 **Christopher A.^c, Vasilatos Charalampos^b, Tsoukalas Nikolaos^a**
7

8 ^a *Centre for Research and Technology Hellas, Chemical Process and Energy Re-*
9 *sources Institute, 15125, Maroussi, Greece, koukouzas@certh.gr*

10 ^b *Department of Economic Geology and Geochemistry, Faculty of Geology and*
11 *Geoenvironment, National & Kapodistrian University of Athens, 15724, Athens,*
12 *Greece, zach-kyp@geol.uoa.gr*

13 ^c *Environmental Science Center, British Geological Survey, Keyworth, NG12*
14 *5GG, Nottingham, England, caro@bgs.ac.uk*

15
16 ***Abstract***

17 Representative sandstone samples from Mesohellenic Trough (NW Greece) were selected
18 to investigate the geochemical reactions that occur when they come in contact with CO₂
19 under representative in-situ conditions (T=70°C, P=150bar, 6 months reaction in batch
20 experiments). Those sandstones consisted of predominant calcite and quartz, with lesser
21 amounts of feldspars, chlorite, ankerite, dolomite, kaolinite, montmorillonite and musco-
22 vite. After reaction with CO₂, the brine became acidic and was enriched in cations as a
23 result of mineral dissolution. Minor mineralogical changes were observed that involved:
24 a) the dissolution of carbonate minerals and b) the incongruent dissolution of chlorite to
25 form clays and silica. The results related to these, have been linked with geochemical
26 modelling using the PHREEQC code. Simulation results for a 10 ka time period predicted
27 that chlorite was expected to dissolve completely within 100 years, leading to boehmite
28 growth and increasing the mass of dolomite. Feldspars were expected to react at a later
29 stage in the reaction sequence. Sensitivity tests were run to access the effect of various
30 adjustable parameters on the outcome results. The geochemical experiments and model-
31 ling lend support to the view that Pentelofos and Tsotyli sandstone formations of the
32 Mesohellenic Trough are suitable for the long-term storage of CO₂ produced in the
33 neighbouring lignite-fired power plants, at least in terms of mineralogy and geochemistry.

34

35

36 *Key words: CCS, sequestration, geological storage, CO₂-brine-rock interac-*
37 *tions PHREEQC*

38

39 **1. Introduction**

40 Progressive industrialization and burning of fossil fuels has caused dramatic increases in
41 emissions of carbon dioxide (CO₂) to the atmosphere in the past decades, leading to inter-
42 national concern about the potential for rapid climate change. CO₂ capture and under-
43 ground storage (CCS) has been proposed as a workable method to reduce emissions to the
44 atmosphere, and play a key role as we transition to low carbon energy supplies (IPCC,
45 2005).

46 Storage can be attained through injection of CO₂ into deep saline aquifers or de-
47 pleted oil/gas reservoirs. In many geological settings, in-situ pressure/temperature condi-
48 tions at greater than 1 km deep mean that CO₂ can exist as a stable supercritical phase
49 (sCO₂, needs to be above 31.1°C and 7.39 MPa). Once injected, CO₂ is contained under-
50 ground through a combination of capillary, structural, solubility or mineral trapping (De
51 Silva et al., 2015; Wigand et al., 2008). However, the selection of suitable reservoirs and
52 their caprocks is not trivial and detailed studies must be carried out to understand the geo-
53 logical conditions and structure of the whole basin (porosity, permeability, geometry, ca-
54 pacity, mineralogy etc.), before proposing it as a potential storage mean. The presence of
55 sCO₂ in geological media can cause a number of geochemical reactions that can potential-
56 ly change the reservoir integrity and trapping potential. Such changes include the acidifi-
57 cation of pore waters, dissolution of primary minerals, precipitation of secondary phases,
58 and changes in porosity and permeability (Black et al., 2014; Gaus, 2010). However, de-
59 tailed assessment of individual formations is required to assess whether these changes
60 result in overall increases or decreases in CO₂ storage potential.

61 Many experimental studies have been conducted in the laboratory (i.e. Alemu et
62 al., 2011; García-Rios et al., 2013; Huq et al., 2012) or in situ (Wigand et al., 2008) to
63 investigate the CO₂ trapping potential of various formations, such as sandstones and lime-
64 stones (i.e. García-Rios et al., 2013), basalts (i.e. Van Pham et al., 2011), granites (i.e. Lin
65 et al., 2008) and shales (i.e. Sorensen et al., 2009). Many of these studies utilised ‘batch’-
66 type reactors, where a fixed volume of solid and brine are placed into a vessel, pressur-
67 ised with CO₂, and then allowed to react for a period of time (Lu et al., 2013;
68 Rathnaweera et al., 2016). Analysis of extracted fluids and solids is used to determine the
69 extent of CO₂-water-rock reaction (see comments in the experimental methods section
70 below). This experimental approach has benefits of relative simplicity and ease of control

71 of experimental parameters, and is good for assessing the types and directions of faster
72 CO₂-water-rock reactions. However, it does not replicate the complex feedback processes
73 that occur between kinetically-controlled dissolution/precipitation processes and fluid
74 transport. These are better simulated in flow experiments (Bateman et al., 2005; Galarza
75 et al., 2013; Huq et al., 2015; Luquot et al., 2012).

76 Sandstones are usually favoured, largely due to their widespread distribution,
77 high permeability, favourable geochemical characteristics (i.e. better long-term pH buffer
78 capacity), and presence of caprocks to keep the buoyant CO₂ within the reservoir rock.
79 However that does not mean that other rock types are unsuitable, and carbonate-
80 dominated rocks, as in the Weyburn case, can also be used (Wilson and Monea, 2005).
81 The resultant alteration depends on the mineralogical composition of the rock sample
82 used, the experimental conditions, and the duration of the experiments. Experimental
83 studies have simulated a variety of in-situ pressure and temperature conditions, as those
84 of the stored CO₂ will vary according to the depth of the target formations and local geo-
85 thermal gradient. Together with the porewater composition (largely its salinity), these will
86 dictate CO₂ solubility, and solution pH. A further factor that might control pH (and poten-
87 tially redox state) will be the types and compositions of impurities in the CO₂-rich phase
88 (e.g. oxygen, sulphur dioxide, hydrogen sulphide). Whilst the potential impact of impuri-
89 ties is beyond the scope of the experiments presented here, some recent studies have at-
90 tempted to quantify CO₂-impurity-brine-rock reactions (i.e. Schoonen et al., 2012; Wilke
91 et al., 2012). For most studies, formation water or simplified brine is usually used as the
92 liquid medium (e.g. De Silva et al. 2015).

93 It is worth noting, that the reactions observed in laboratory experiments are not
94 always the same as those seen in natural CO₂-rich settings or field injection operations,
95 and care must be taken when extrapolating experimental results to field conditions. In
96 part, these differences result from the very different durations over which reactions occur,
97 with laboratory experiments capturing detailed information on short-term processes, and
98 natural systems reflecting the end points of reactions which may have been ongoing for
99 thousands or millions of years. Some investigators have used significantly elevated tem-
100 peratures to increase the rates of CO₂-water-rock reactions (Kaszuba et al., 2003; Lu et
101 al., 2013) and overcome sluggish reaction kinetics. Whilst this can be a useful approach
102 to test models, potentially it risks the formation of secondary phases that would not be
103 found within sedimentary used for CO₂ storage. Furthermore, the conditions in large scale
104 field experiments are less controlled than in laboratory reactors, and factors such as flu-
105 id:rock ratio and fluid flow rates may vary greatly within different parts of a formation.
106 Moreover, mineralogical and structural heterogeneities may mean that the (relatively
107 small) rock samples used in the laboratory are not always representative of the whole
108 formation. Indeed, samples used in laboratory experiments are typically pretreated (e.g.
109 crushed, sieved and washed with acetone). Whilst this may increase homogenisation, and
110 also increase surface areas to accelerate reaction rates (Huq et al., 2012), it will not reflect

111 the often complex porosity/permeability of real rocks. Factors such as heterogeneity,
112 permeability and porosity of the rock must be taken into account when extending the re-
113 sults of laboratory experiments to study the reaction and transport of sCO₂ and/or CO₂-
114 saturated brine to field scales.

115 The Mesohellenic Trench has been attracted scientists' interest for further study
116 unravelling the issues for potential CO₂ storage for many reasons. In particular, the area
117 represents an appropriate geological environment of basin for CO₂ storage (Koukouzas et
118 al., 2009). The size of the basin is remarkable, reaching up to 25000 km², having signifi-
119 cant thicknesses of layers in a range of 1500-3500 m. Voluminous formations of sand-
120 stones and conglomerates are deformed in open anticline structures, representing possible
121 porous reservoir rocks. In addition, marls and clays overlying the previous formations are
122 excellent impermeable accumulations, forming the cap rocks of the whole stratigraphic
123 succession. The tectonic stability characterizes the area, corresponding to a substantial
124 factor favoring the storage of CO₂. Moreover, the proximity of the basin to significant
125 CO₂ emission sources of the adjacent lignite power plants (there exist the largest of the
126 Public Power Corporation's lignite-fired power plants are located representing 70% of the
127 country's total power and heat production), as well as the possible existence of hydrocar-
128 bons (the 64% of the lignite reserves of the country (~2.8 Gt) are hosted in the same re-
129 gion) are two more criteria that lead us to a thorough study of the Mesohellenic Trench in
130 such perspective (Koukouzas et al., 2009).

131 The aim of the present study is to investigate the potential mineralogical evolu-
132 tion of representative sandstone samples from the Mesohellenic Trough (NW Greece)
133 exposed to a brine saturated with sCO₂. The current work included: a) laboratory experi-
134 ments with crushed sandstone samples, and b) extending observed reactions to longer
135 timescales using geochemical modelling. The fluid composition and sample mineralogy
136 were studied before and after the reactions with the CO₂-saturated brine to investigate the
137 geochemical reactions that may take place within a potential CO₂ storage reservoir. The
138 experimental results were used to help define geochemical reactions which were extrapo-
139 lated to longer timescales using the PHREEQC geochemical code. The ultimate goal is to
140 predict the mineralogical evolution of the sandstones over long time-scales (i.e. 10 ka), in
141 order to assess their potential for CO₂ geological storage.

142

143

144 **2. Materials and Methods**

145 **2.1. Materials**

146 The sandstone samples used in the current experimental work come from the molassic
147 formations of Mesohellenic Trough (MT). The MT is a basin with a length of over 200

148 km and a width of 30-40 km in NW Greece and it was developed between Middle Eocene
149 to Late Miocene and has a NNW-SSE orientation (Figure 1, modified after Brunn, 1956).

150

151

Insert Figure 1

152

153 The sedimentary formations of the basin include deltaic conglomerates, alluvial
154 scree, sandstones and clays of turbiditic and deltaic origin, floodplain and sandy shelf
155 sediments, with a maximum thickness of 4,000 meters. The Tsotyli and Pentalofos For-
156 mations, correspond to potential local caprock and reservoir respectively. The Tsotyli
157 Formation (23-21 Ma) consists of turbiditic conglomerates, sandstones and shales. The
158 Pentalofos Formation (25-23 Ma), consists mainly of loam and fine-grained sandstones
159 (Vamvaka, 2009; Zelilidis et al., 2002). The two sandstone samples that were used in the
160 experiments came from surface outcrops of the Tsotyli (TS) and Pentalofos (PS) For-
161 mations respectively.

162

163 **2.2. Experimental set up and procedure**

164

165 Each sandstone sample was gently crushed and sieved to give 3 size fractions (<250, 250-
166 500 and >500 μm). The 250-500 μm fraction was selected for use in the experiments.
167 This was largely as a compromise between being fine enough to have a high enough sur-
168 face area to cause sufficient reaction on an experimental timescale, and coarse enough to
169 facilitate mineralogical observations. The grains were rinsed with acetone to remove fine
170 particles, and filtered using a Buchner funnel containing a Whatman no.1 filter paper. 20g
171 of this granulated and cleaned sandstone was mixed with 200 ml of ~0.5M NaCl solution
172 (simplified porewater) (fluid/rock mass ratio 10:1). To minimise corrosion and potential
173 contamination issues, the reaction vessel consisted of lower and upper wetted parts made
174 of titanium, and these were held together with a 316 stainless steel retaining ring. A Viton
175 O-ring was used as a pressure seal. A magnetic stirrer was used to ensure good mixing
176 between fluid and solid. However, in order to minimise mechanical damage to the solid
177 grains, this stirrer was held in a small cage just above the bottom of the vessel. A titanium
178 dip tube to the bottom of the reaction vessel allowed for the withdrawal of aqueous sam-
179 ples. Once assembled, the vessels were heated in a fan-assisted Binder oven to 70 °C
180 (manufacturer's data show temperature fluctuations less than $\pm 0.5^\circ\text{C}$). The salinity cho-
181 sen (approximate seawater salinity) has also been applied by a number of authors in
182 their experiments (Baraka, 2015; De Silva et al., 2015; Zhang and Pu, 2011). In order to
183 ensure good rock-fluid mixing, it was stirred via a magnetic stirrer for 2 minutes every 4

184 hours. Periodic, rather than continuous, stirring ensured that the sandstone powder did not
185 suffer too much mechanical abrasion, but also ensured that the reactants were well mixed
186 during the experiment.

187 For the initial 37 days of the experiment the sandstone and solution were allowed
188 to partially equilibrate under CO₂-free conditions, with 15 bar (1.5MPa) pressure of inert
189 nitrogen in the headspace of the reaction vessel to aid sampling of the brine. Prior to
190 aqueous sample collection, 1-1.5 ml was withdrawn and discarded in order to clean the
191 sampling lines. The volume of the collected sample was typically 10 ml. By day 37 the
192 brine had been sampled twice, and this was followed by depressurisation and flushing of
193 the headspace (at 70°C) with excess CO₂ to remove the nitrogen. Once flushed, the CO₂
194 pressure was raised, and thereafter maintained at a pressure of 150 bar (15 MPa - super-
195 critical CO₂ conditions) for the rest of the experiment using a Teledyne ISCO 500D pump
196 running in constant pressure mode. Eight further brine samples were taken between then
197 and the end of the experiment, whilst the experiment was under CO₂-pressurised condi-
198 tions. During sampling, the CO₂-rich brine was allowed to degas into a sterile syringe.
199 The collected samples were pre-filtered through an Acrodisc NYLON 0.2 µm filter. The
200 associated loss of CO₂ will have an unavoidable impact on very rapidly-responding geo-
201 chemical parameters - such as pH. However, after sampling the solutions were rapidly
202 analysed for Eh and dissolved bicarbonate, as these would change if the solutions were
203 left for some time. Other subsamples were immediately preserved for the accurate deter-
204 mination of reduced iron using 2,2-dipyridyl, and major and trace cations using a 1% ad-
205 dition of concentrated nitric acid. The addition of acid prevented the possible precipita-
206 tion of solids which might occur during storage once the samples were fully degassed.
207 Immediately prior to analysis, the fluid samples were checked visually, and no precipi-
208 tates were observed. It has been our experience that collection of several subsamples in
209 this way, together with the immediate analyses of key parameters, gives an accurate rep-
210 resentation of most in-situ fluid compositional parameters. The main exceptions to this
211 are: a) total dissolved inorganic carbon, as much of the dissolved CO₂ (CO_{2aq}) will degas,
212 b) pH, as this will be influenced by the amount of dissolved CO₂ in solution. However,
213 geochemical modelling can be used to effectively 'titrate' the lost CO₂ back into solution.

214 A total of ten fluid samples (having an accurately-known volume between 10-15
215 ml) were collected from each vessel. Pressure stayed relatively constant within the vessel
216 during the sampling procedure because the CO₂ pump ran in constant pressure mode, and
217 added extra CO₂ as brine was withdrawn. The periodic sample extraction led to modifica-
218 tion of the liquid/solid ratio from 10:1 to approximately 4:1 at the end of the experiment.
219 The impact of this changing fluid:rock ratio would have been an apparent increase in the
220 rate of reaction, and would thus have helped drive the reactions closer to steady-state
221 conditions. This was advantageous to this study in order to assess dissolution/precipitation
222 processes and overall reaction directions. However it makes quantifica-
223 tion of rates of mineral reactions more difficult.

224 After a total duration of 184 days (6 months) as much as possible of the remain-
225 ing brine was drained from the experiment via the ‘dip tube’ that reached close to the bot-
226 tom of the vessel. It was then slowly depressurized and dismantled to allow the collection
227 of the solid material. Removal of brine prior to depressurization was done to minimize the
228 potential for unintended carbonate mineral precipitation (Figure 2).

229

230

Insert Figure 2

231

232 **2.3. Mineralogical analysis**

233 Quantitative mineralogical analysis of the samples before and after the reaction with CO₂
234 was achieved by powder X-Ray Diffraction analysis (XRD) using a SIEMENS D5005
235 instrument (CuK α radiation operating at 40kV and 40mA), with 2 θ angle ranging from 5°
236 to 70°, step 0.01°, time per step 5sec, at ambient conditions. Mineralogical evaluation was
237 conducted using the Siemens DIFRAC PLUS v2.2 software by Siemens and data were
238 processed using the Rietveld method by the BRUKER TOPAS Software. The morpholo-
239 gy of the samples was examined by scanning electron microscopy (SEM) using a JEOL
240 JSM-5600 instrument, operating at 25-30 kV.

241 **2.4. Chemical Analysis**

242 Each sample was sub-sampled and prepared for analysis of pH, Eh (redox), anions, cati-
243 ons, alkalinity and iron (II) using the following methods. pH on depressurised (i.e. largely
244 CO₂ degassed) solutions was measured at room temperature and pressure by an Orion
245 bench top meter and glass pH electrode calibrated using NBS-traceable pH buffers of 4, 7
246 and 10 prior to sample analysis. The calibration of a Ag/AgCl Eh electrode was checked
247 using Zobell’s solution prior to analysis of Eh. Alkalinity was measured using potentiom-
248 etric titration as soon as possible after sampling (usually within 1-3 days). The remainder
249 of the subsamples were first pre-filtered through a 0.2 μ m nylon Acrodisc filter. Subsam-
250 ples destined for cation analysis were preserved by acidification with 1% concentrated
251 nitric acid. Subsamples for anion analysis could not be preserved, but were diluted to
252 25% concentration with deionised water to minimise the potential for precipitation prior
253 to analysis. The cation, anion and iron (II) samples were stored in a fridge at 4°C prior to
254 analysis. Cations were analysed using ICP-MS (dilution 1:10 for Ca, Mg, Na and K), ani-
255 ons by ion chromatography and reduced iron by UV-visible spectrophotometry.

256 **2.5. Geochemical modelling and reaction rates**

257 The PHREEQC v.3.3 geochemical code was employed to simulate the reactions in the
258 solid/liquid interface between the sCO₂-saturated brine and the sandstone samples. The
259 LLNL database was used (compiled by Lawrence Livermore National Laboratory) which

260 employs the Truesdell-Jones model to calculate the activity coefficients at high ionic
261 strengths (up to 2) (Delany and Lundeen, 1991; Parkhurst and Appelo, 1999).

262

263

Insert Figure 3

264

265 Reaction rate parameters for each mineral were defined and solved by CVODE
266 solver for stiff ordinary differential equation (ODE) systems. The methodology followed
267 is summarized in Figure 3. Speciation calculations were conducted on the basis of
268 measured final solution composition regarding the major ions (total Ca, Mg, Na, K, Al,
269 Si, Fe) and total inorganic carbon, taking into account the loss in solution mass and the
270 degassing effects due to sampling. Kinetic and equilibrium models accounted for possible
271 changes in total mass of the solids during the experiment.

272 Reaction dissolution and precipitation rates were calculated using the Transition
273 State Theory (TST) (Lasaga, 1984) and presented in detail in Appendix A. The
274 thermodynamic parameters and kinetic rate data of the selected minerals are compiled
275 and presented in Appendix A. Most of them are included in llnl.dat database. The
276 composition of ankerite chosen in the present work was a solid solution consisting of
277 40% dolomite and 60% ankerite as end-members, giving the formula $\text{CaFe}_{0.6}\text{Mg}_{0.4}(\text{CO}_3)_2$
278 and the thermodynamic data used, were taken from Van Pham et al. (2012).

279 Moreover, some additional phases were tracked in the model to investigate their
280 potential for formation. These phases include magnesite, siderite, dawsonite, boehmite,
281 $\text{Fe}(\text{OH})_3$, goethite, gibbsite and illite. As kinetic data for ankerite and dawsonite could not
282 be identified in the literature, the respective parameters of another carbonate phase,
283 dolomite, were taken as being similar, and were used instead. Respectively, siderite data
284 were used for magnesite, boehmite for hydro-oxides and kaolinite for clays (Marty et al.,
285 2015; Palandri and Kharaka, 2004; Van Pham et al., 2011).

286 **3. Results & Discussion**

287 **3.1. Mineralogy of the reactant and produced solids**

288 Both of the sandstone samples are arenites and mainly consist of well-rounded, fine-
289 grained quartz and feldspars grains. These lie within a diagenetic carbonate cement that
290 consists of both calcite and dolomite, with calcite being the more abundant (Figures 4 &
291 5).

292

293

Insert Figure 4

294

295 The silicate grains of the Tsotyli Formation (TS) sample are anhedral and smaller
 296 than 100 μm . The phyllosilicate minerals detected are chlorite and muscovite having nar-
 297 row flaky grains of about 50 μm long. Calcite and dolomite appear in the form of relative-
 298 ly large anhedral crystals. Opaque minerals appear as rare and small-sized grains. Limited
 299 fossil fragments were found and identified to be *Operculina* sp..

300 The sample of the Pentalofofos Formation (PS) is a poorly to moderately sorted
 301 sandstone that consists of larger silicate (200-500 μm) and carbonate (50-500 μm) grains.
 302 These lie within an authigenic matrix of clay minerals including illite, kaolinite and smec-
 303 tite (10-50 μm). It exhibits a wide range of sizes, mostly with angular grains although few
 304 are subrounded. Phyllosilicate grains vary in size between 10 and 500 μm . Feldspar min-
 305 erals include both alkali feldspars as well as plagioclase. Additional mineral phases in-
 306 clude biotite, partly altered to chlorite, muscovite, as well scarce small olivine grains.

307

308

Insert Figure 5

309

310

Insert Figure 6

311

312

313 XRD analysis confirmed the microscopic observations, that both samples exhibit a com-
 314 mon mineralogical composition (Figure 6 & Table 1). The bulk of the samples are com-
 315 posed mainly of calcite, quartz and feldspars, with the phyllosilicates of lower abundance
 316 in the sandstones. The main differences in the mineralogy of the two samples are (a) the
 317 presence of ankerite in the TS sample and montmorillonite in the PS sample, and (b) the
 318 high calcite content in the TS sample.

319

320

321 Table 1: *Quantitative X-ray analysis (wt%) of the samples before and at the end of the*
 322 *interaction with CO₂-saturated brine, as well as the expected percentages calculated by*
 323 *the kinetic reaction models of Section 3.3.3.*

Sample	Pentalofofos Sandstone (PS)			Tsotylli Sandstone (TS)		
	Unreacted	CO ₂ -	Kinetic	Unreacted	CO ₂ -	Kinetic
Minerals						

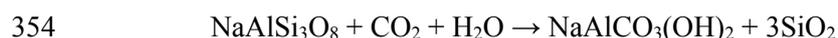
	Sample	reacted sample	model results	Sample	reacted sample	model results
Albite	15	13	15.6	~9	~9	9.4
Calcite	38	35	35.6	58	58	57
Clinochlore	7	6	6.6	4	2.5	3.2
Dolomite	4	2	3.6	<0.5	2	0.12
Kaolinite	<0.5	<0.5	0.5	1	1	1.1
Montmorillonite	3	4	3.1	-	-	-
Muscovite	~2	~2	1.8	~0.5	<0.5	0.4
Orthoclase	10	10	10.7	5	5	5
Quartz	~21	~28	22.4	17	17	17.7
Ankerite	-	-		6	5	6.1

324

325 The interaction of the samples with CO₂-saturated brine only resulted in minor
326 mineralogical changes over the duration of the experiments. This is not entirely surprising
327 given the relatively slow reaction kinetics at the experimental temperatures. Changes ob-
328 served include decreasing of feldspars' quantity and a relative change in the proportion of
329 carbonate phases. Minor changes were also observed in the amounts of chlorite and mus-
330 covite. Those minor changes may be due to the incongruent dissolution of feldspars and
331 phyllosilicates leading to clay formation (Black et al., 2014; Kaszuba et al., 2013). How-
332 ever, SEM observation of the powder fraction that was used in the experiments was una-
333 ble to confirm those mineralogical changes. The magnetic stirrer bar from sample PS at-
334 tracted some iron bearing grains, which could also be of primary origin. No new second-
335 ary phases (such as Fe/Al hydro/oxides dawsonite, magnesite, etc.) were identified by
336 XRD or SEM analysis. Although dawsonite formation is favoured in some feldsparic ra-
337 ther than in quartz sandstones (Tremosa et al., 2014), its absence in experimental studies
338 is in line with other studies. The dissolution/transition among the carbonate minerals and
339 the incongruent hydrolysis of aluminosilicates, mainly feldspars, to clays have been well
340 documented in other CO₂-water-rock reaction studies (Kaszuba et al., 2013; Lu et al.,
341 2013; Wigand et al., 2008). In the Wekerdam gas field, the mineralogical study conclud-
342 ed that feldspar hydrolysis promoted the transformation of kaolinite to illite, whereas do-
343 lomite and siderite are the main carbonate precipitates (Koenen et al., 2013). When sand-
344 stone samples from the Songliao Basin in China were subjected to laboratory experiments
345 simulating reservoir conditions (T=100°C, P=24MPa), complete dissolution of calcite and
346 partial hydrolysis of feldspars occurred, together with enrichment in quartz and clays (Yu
347 et al., 2012). Although our study considers temperatures at <100°C, the importance of
348 CO₂-feldspar reaction and resultant clay formation is also highlighted by higher tempera-

349 ture work at up to 200°C involving both sandstones (Kaszuba et al., 2003; Lu et al., 2013)
350 and granite (Lin et al., 2008).

351 None of the above studies reported the precipitation of dawsonite, although it is a
352 possible precipitate coming from hydrolysis of feldspars in sodium-rich solutions (De
353 Silva et al., 2015):



355 *Albite* *Dawsonite* *“amorphous”*

356 Dawsonite has been considered an important secondary phase in modelling studies, large-
357 ly because its relatively large molar volume might have an impact on porosity/
358 permeability (Johnson et al., 2004). Indeed, it has been reported in some sandstone
359 formations that have come into contact with CO₂ under elevated pressure and temperature
360 (Worden, 2006; Zhou et al., 2014). In some cases its formation was also related to alka-
361 line Na-HCO₃ waters (Kampman et al., 2014), though in others to acidic high-salinity
362 brines (Worden, 2006). However, its formation has been questioned because of its ab-
363 sence in many natural settings (Hellevang et al., 2011) and general absence in laboratory
364 experimental studies even when it was expected to be found, including when a pure feld-
365 spar sample was used (Alemu et al., 2011; Gaus et al., 2005; Huq et al., 2012; Van Pham
366 et al., 2011; Wigand et al., 2008). There is thus some uncertainty as to why dawsonite
367 does not form in some environments, but possible reasons could include kinetic con-
368 straints, temperatures being too high, or pH being too low (Hellevang et al., 2011; Lu et
369 al., 2013).

370

371

372 **3.2. Fluids chemistry**

373 The concentrations of major ions and selected trace elements for both experiments are
374 presented in Table 2 for the starting brine composition, N₂-saturated brine (0-37 days),
375 and also CO₂-saturated brine (37-184 days). The pH and Eh of the starting solution drop
376 after addition of CO₂:



378 However, it is noted that the measured pH values refer to solutions that have been largely
379 degassed.

380 The major element chemical evolution of the extracted fluid samples is presented
381 in Figure 7 and Table B.1 (Supplementary Material). Complete chemical analyses of the
382 fluid samples are available in Appendix B. Initial brine-sandstone interaction leads to a

383 slight increase in ion concentrations in the solution of both sandstones (Ca~70-110mg L⁻¹,
 384 Mg~7-12mg L⁻¹, K~5-12mg L⁻¹, HCO₃⁻ ~60-100 mg L⁻¹), likely due to dissolution of
 385 carbonates and possible ion exchange effects on clay surfaces (Table 2). Si reaches 7-8
 386 mg L⁻¹ and Al 20-100 μm L⁻¹ respectively, as a result of minor dissolution of the aluminosilicates,
 387 especially muscovite and clinocllore. The TS sample exhibits higher dissolved
 388 Fe concentrations (up to 3.5 mg L⁻¹) due to dissolution of ankerite.

389 Once CO₂ enters the reaction vessel, ion concentrations increase abruptly. Ca,
 390 and bicarbonate concentrations reach ~1200 mg L⁻¹ and ~1500 mg L⁻¹ within the first 3
 391 days, as a result of the brine acidification and calcite/dolomite dissolution. K reaches 6
 392 mg L⁻¹ and 16 mg L⁻¹ in the TS and PS sample experiments respectively, considered
 393 mainly due to muscovite hydrolysis. Magnesium was increasing steadily in both samples,
 394 whereas aluminum and silica contents increased only to a small extent, as hydrolysis re-
 395 actions are relatively slow, making them hard to quantify over low temperature experi-
 396 mental time-scales of just a few months (Gaus, 2010).

397

398

Insert Figure 7

399

400 The overall concentration of ions released reached approximate steady state with-
 401 in the first ~50 days of the experiment, similar to those reported by Wigand et al. (2008)
 402 (~33 days at T=60°C, P=150 bar) and Kaszuba et al. (2003) (~55 days at T=200°C,
 403 P=200bar). Only Mg shows a significant steady increase in concentration with time. It is
 404 noted that the reduction of brine:rock ratio due to constant fluid extraction may help con-
 405 tribute to the Mg, K, TIC and Si enrichment of the final solution because of condensation.

406 The time-dependent trend of selected variables was examined through Pearson
 407 correlation analysis according to their correlation coefficient R given by the equation (Eq.
 408 1):

409
$$r = \frac{\sum x_i y_i - n\bar{x}\bar{y}}{\sqrt{(\sum x_i^2 - n\bar{x}^2)} \sqrt{(\sum y_i^2 - n\bar{y}^2)}} \quad (1)$$

410 Bicarbonate and Ba-Sr-Mn (R>0.8) shows a strong dependence of these elements
 411 with dissolution/precipitation of carbonate minerals. Moreover, the relationship between
 412 Co-Ni-Mn (R>0.9) can be attributed to either the ophiolitic protolith mineral phases that
 413 contribute to the sandstone composition, or the presence of Mn hydroxides (Wigand et
 414 al., 2008). Fe is not correlated to any of the major or trace elements analyzed for. Iron
 415 could be present in the lattice of carbonates, or originate from chlorite and olivine, but

416 neither case was included in the proposed models. The presence of olivine grains was
417 confirmed in SEM images, although in trace amounts.

418 Sodium exhibits different behavior between the two samples, showing positive
419 correlation to Si ($R=0.9$) in the TS experiment and negative correlation in the PS experi-
420 ment ($R=-0.9$), which can be attributed to the minor differences in mineralogy of the
421 sandstones. For the PS sample, incongruent dissolution of albite releases sodium that
422 could be bound into a montmorillonite precipitate, unlike the TS sample that lacked any
423 major clay components (Table 2).

424

425

Table 2: *Chemical analysis of the extracted fluids*

Analyte	TS			PS	
	Starting solu- tion	Brine with N ₂ after 37 days	Brine with sCO ₂ after 184 days	Brine with N ₂ after 37 days	Brine with sCO ₂ after 184 days
pH (at 20°C)^a	8.96	7.51	6.68	7.48	6.71
Eh (mV at 20°C)	137.4	109.4	43.5	91.3	13.6
(mg L⁻¹)					
Ca	<10	84	1195	108	1052
Mg	<0.8	9.5	102	12.3	223
Na	12940	11676	12395	13538	11943
K	1.2	4.8	6.4	12.3	15.4
HCO₃⁻	-	157	2714	90	2894
Cl⁻	17230	17546	18589	16972	18758
TIC	0	31	534	18	570
Si	<1.7	8	40	8	108
Balance (%)	7	1	-9	10	-12
(µm L⁻¹)					
Ba	<5	122	567	53	233
Sr	9	805	4639	200	879
Mn	<7	99	870	115	2033

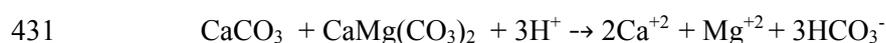
Total Fe	<42	1546	1930	3344	2062
Li	<37	65	96	46	88
Al	<18	23	48	19	<18
Ti	<0.6	<0.6	1.1	<0.6	1.1
V	<3	<3	4	<3	5
Cr	<1	<1	2	<1	6
Co	<0.4	17.7	37.1	3.8	83.9
Ni	0.8	668	696	147	1397
Cu	4.2	4.2	20	23.7	3
Zn	20	23	40	23	43

426 ^apH values refer to degassed solutions after sampling

427 Combining the mineralogical and chemical data of the samples, the proposed re-
428 actions include:

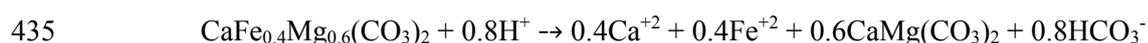
429 i. Dissolution of carbonates:

430 In PS sample both calcite and dolomite dissolved releasing Ca and Mg.



432 Calcite Dolomite

433 In TS sample, dissolution of calcite was not observed (at least, not detected according to
434 Rietveld method). Instead, ankerite transition into dolomite was proposed as:



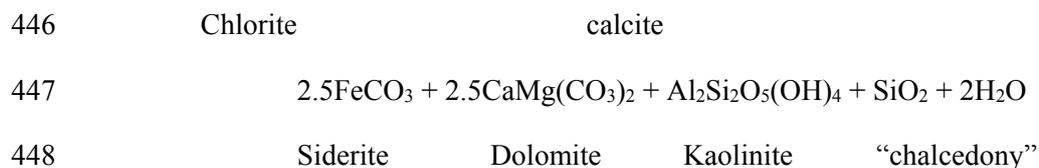
436 Ankerite Dolomite

437 As Ca reached a steady state very quickly (within ~4 days after CO₂ injection) in both
438 samples, it was assumed that the respective Mg concentration at equilibrium should not
439 exceed ~40 mg L⁻¹, and thus the excessive amount had a different origin.

440 ii. Hydrolysis of phyllosilicates (clinochlore/muscovite):

441 The excess Mg amount was attributed to clinochlore hydrolysis, as testified by numerous
442 researchers (e.g. Alemu et al., 2011; Black et al., 2014; Luquot et al., 2012). Gaus (2010)
443 proposed that chlorite may interact with calcite and CO₂ to form siderite, dolomite, kao-
444 linite and amorphous silica:





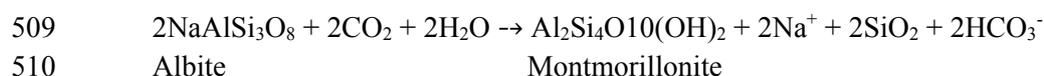
449 In our study, calcite dissolved along with dolomite in PS sample. Siderite was not ob-
 450 served and kaolinite mass remained the same. Even if the proposed reaction would have
 451 occurred, the small mineral amounts produced, would not be detected by the deployed
 452 methods (XRD or SEM).

453 Potassium may have come from minor muscovite corrosion from the brine. The almost
 454 fixed concentration during CO_2 diffusion suggested no further interaction of the phase
 455 with the solution.

456 iii. Precipitation of montmorillonite:

457 In some studies montmorillonite was directly associated with the hydrolysis of albite
 458 (Fischer et al., 2011; Huq et al., 2012; Wigand et al., 2008) and a simplified reaction can
 459 be expressed as:

460



511 Montmorillonite growth occurred only in PS sample, where albite mass showed some de-
 512 crease. On the contrary, is absent in TS sample, where albite mass remained constant.
 513 Thus, it was assumed that montmorillonite was a byproduct of albite hydrolysis.

514 The above reactions were confirmed both experimentally and numerically and were con-
 515 sistent with those refereed in the literature concerning siliciclastic formations (Horner et
 516 al., 2015; Huq et al., 2015).

517

518

519 **3.3. Geochemical Modelling**

520 **3.3.1. Fluid speciation**

521 Based on the chemical evolution of the analyzed brine samples, saturation indices were
 522 calculated for the mineral phases within the rocks, plus some possible secondary precipi-
 523 tates. The measured pH values of the brine samples extracted during the CO_2 -pressurised
 524 part of the experiments were recalculated by equilibrating them with CO_2 ($\log P_{\text{CO}_2} = 2.17$)
 525 to reproduce the experimental conditions. Thus, the pH values calculated in this manner,

526 do not exceed 4.8, and the saturation indices were calculated using these values (Figure
527 8).

528 *Insert Figure 8*

529

530 Prior to CO₂ injection, the analyzed fluids appear undersaturated with respect to
531 all major mineral phases. After interaction with the brine, calcite, dolomite, chlorite, and
532 quartz are close to equilibrium, with saturation index (SI) values ranging from -0.6 to 0.6.
533 When the sCO₂ entered the system, the analyzed fluids become oversaturated in respect
534 to kaolinite (SI>2), montmorillonite (SI>1) and muscovite (SI>2) and undersaturated with
535 respect to feldspars (SI>-2). This trend reflects the incongruent dissolution of chlorite
536 discussed previously, as well as the minor hydrolysis of albite to montmorillonite (in PS
537 sample), and is in line with previous models (Gunter et al., 1997, 1993). Muscovite pre-
538 cipitation would never occur, however it could be considered as substitute for illite pre-
539 cipitation.

540 The fluid samples from both experiments are almost equilibrated with calcite,
541 quartz and dolomite.

542 The saturation state of some possible secondary precipitates was also calculated.
543 Both experiments were close to equilibrium with respect to boehmite, gibbsite, magnesite
544 and siderite, prior to CO₂ injection. When CO₂ entered the system, the fluids became
545 oversaturated with respect to boehmite (SI~ 1.5), illite (SI~ 0-2), Fe-hydro/oxides
546 (SI>2.5) and dawsonite (SI>1.5), and undersaturated in respect to magnesite (SI> -1.5)
547 and siderite (SI> -3). These phases were also included in the kinetic models.

548

549 **3.3.2. Model input parameters**

550 Mineral reaction kinetics depends on a number of parameters, of which some were calcu-
551 lated or measured experimentally, whilst others were available in the existing literature
552 (i.e. Marty et al., 2015; Palandri and Kharaka, 2004; Van Pham et al., 2011).

553 Mineral surface areas S_A (m² g⁻¹) were calculated assuming that all grains were
554 spherical (i.e. geometric areas, and done for reasons of simplicity, though we
555 acknowledge that this is not truly realistic for phyllosilicate minerals) and their grain di-
556 ameter was estimated from SEM images (Appendix A) (Tester et al., 1994). This is a
557 simplistic approach, as there is no account for surface roughness, and thus our assumption
558 will tend to minimize surface areas. On the other hand, only the more reactive surface
559 sites will actually undergo dissolution. The role of reactivity of the surface area was ac-
560 cessed through a number of sensitivity simulations given in Section 3.4.2. The effective
561 diameter, d_e , (calculated using equation A6, in Appendix A according to (Tester et al.,

1994) and mass amount in moles, n , is shown in Table 3. Reactive fraction λ was set to 1 for all aluminosilicates, assuming that the small grain size of the solids and their unconsolidated form, allows for the whole grain surface to come in contact with the solution. However, this value initially led to overestimation of Ca and Mg concentrations, and λ was subsequently set to 0.001 for carbonate phases.

Table 3: Mineral parameters for the kinetic modelling

Mineral	PS				TS		
	ρ (g cm^{-3}) (Smyth and McCormick, 1995)	moles	d_e (μm)	S_A ($\text{m}^2 \text{g}^{-1}$)	moles	d_e (μm)	S_A ($\text{m}^2 \text{g}^{-1}$)
Albite	2.62	0.0113	327	0.007	0.0068	72	0.0317
Orthoclase	2.56	0.0073	327	0.007	0.0036	72	0.0325
Calcite	2.71	0.0763	195	0.011	0.1159	144	0.0153
Dolomite	2.65	0.0038	195	0.012	0.0004	144	0.0136
Montmorillonite	2.35	0.0016	25	0.103	-	-	-
Kaolinite	2.60	0.0004	25	0.093	0.0008	72	0.0320
Muscovite	2.82	0.0010	195	0.011	0.0003	72	0.0295
Clinocllore	2.65	0.0025	195	0.012	0.0014	72	0.0314
Quartz	2.62	0.0699	72	0.032	0.0566	72	0.0317
Ankerite	3.05	-	-	-	0.0058	144	0.0136

567

The effect of ion exchange was also considered in the modelling, although the CEC of the samples was not measured experimentally. The relative ion exchange capacity was calculated using literature CEC values (meq kg^{-1}) for each mineral phase present (kaolinite, montmorillonite, chlorite) and their relative abundance in the samples (Appelo and Postma, 2005). The calculated CEC range from 31 to 67 meq kg^{-1} for the PS sample and from 4 to 16 meq kg^{-1} for the TS sample. The average values used are 50 meq kg^{-1} (5 mmol L^{-1}) and 10 meq kg^{-1} (1 mmol L^{-1}) for the PS and TS samples respectively.

All simulations took into consideration the experimental conditions. The fugacity coefficient and solubility of CO_2 in 0.5M NaCl were calculated as 0.57 and 0.78 $\text{mol/kg H}_2\text{O}$ respectively (Duan & Sun 2003; Duan et al., 1995).

578

579 3.3.3. Equilibrium and kinetic modelling

580 Whilst we recognize that the six-month experiment duration was a relatively short period
581 of reaction time, it is informative to undertake these calculations to ascertain which reac-
582 tions may have neared steady state conditions. An ‘equilibrium model’ was used to simu-
583 late reactions of the rocks with the brine (for up to day 37 of the experiments). It consid-
584 ered equilibrium with calcite, dolomite, chlorite and quartz, and was based upon their re-
585 spective SI values. Cation exchange capacity was also used to study the effect of the clay
586 content of the samples in the chemistry of the fluids. Some degree of secondary precipita-
587 tion (e.g. boehmite for both the PS and TS simulations, and $\text{Fe}(\text{OH})_3$ for TS simulations)
588 was allowed, to counterbalance the increased concentrations of Al and Fe ions in the simu-
589 lated fluids. Furthermore, a kinetic model was used to simulate geochemical reactions
590 after the injection of CO_2 . CEC and λ values remained stable. The model assumed a con-
591 stant CO_2 pressure of 150 bar (15 MPa). Calibration of both models was done by compar-
592 ing the simulated concentrations of major ions with those measured in the sampled fluids.

593 The measured and calculated ion concentrations are shown in Figure 7, and the
594 models were able to broadly reproduce the measured cation concentrations. At a more
595 detailed level however, the model more accurately represented the PS compared to the TS
596 experiment, in which Mg and Si contents were slightly overestimated.

597 The chemical evolution of the fluids reflected the respective mineralogical
598 changes in each sample (Figure 9, Table 1). In general terms, as CO_2 was added to the
599 system, calcite and chlorite were readily dissolved, releasing magnesium and calcium
600 (Figure 9a, b). Dissolution of dolomite (in the PS experiment) or ankerite (in the TS ex-
601 periment) was inferred by rising magnesium concentrations, but was hard to confirm ex-
602 perimentally due to the low mineral content. Feldspars showed little reaction on these
603 timescales. Overall, both systems reach approximate steady state after 50 days of reaction
604 (Figure 9c, d).

605 *Insert Figure 7*

606

607 Excessive chlorite hydrolysis during the simulations gave Al concentration values
608 far greater than those measured. The formation of aluminium colloids which were re-
609 moved from the fluid samples during filtration could be the explanation for the low Al
610 concentrations measured. This increase was counterbalanced by equilibration with
611 boehmite in both models for both solids. The rest of the secondary phases used (i.e.
612 gibbsite, magnesite, dawsonite, illite, etc.) were included in the model with kinetic con-
613 trol. Simulations results suggest that boehmite, gibbsite and $\text{Fe}(\text{OH})_3$ should precipitate in
614 both sandstone samples (Figure 9e,f). However, the amounts predicted fall under the 1%
615 detection limit of the XRD analysis, explaining their apparent absence from XRD pat-
616 terns. Potential secondary carbonate phases (dawsonite, siderite and magnesite) were also

617 included in the proposed models, but the fluids were undersaturated with respect to these
618 phases.

619 The samples also exhibit similar trends with regard to the cation distribution among the
620 exchangeable sites (Figure 9g, h). Sodium occupies 93-95% of the sites at the start of the
621 experiment, which is gradually replaced mainly by Ca, but also by Mg and K. After addi-
622 tion of CO₂, the rapid enrichment of Ca ions in solution enhances replacement of Na ions
623 on the solid surface. Under steady-state conditions, the exchangeable sites consist of 55-
624 59% Na, 37-40% Ca and 4-5% Mg.

625

626

627 **3.3.4. Prediction model**

628 The kinetic model above was extended to simulate potential longer-term reactions with
629 CO₂ – in this case 10 ka. Similar predicted timescales have been used previously by sev-
630 eral researchers (e.g. Hellevang et al., 2013; Mohd Amin et al., 2014; Van Pham et al.,
631 2012). We recognize that this extends an experimentally-derived model far in excess of
632 its validated time period, and the results should be seen as tentative. However, this can be
633 a useful exercise, as it helps identify a possible scenario for the long-term fate of stored
634 CO₂ and its potential impact on the rock types studied.

635 The geochemical reactions predicted for both sandstone samples proceeded very
636 slowly, and in a similar manner (Figure 10a-d). The main reaction was chlorite hydrolysis
637 which enriches the solution in Mg (up to 500 mg L⁻¹), until the chlorite was exhausted at
638 100 years of simulated time. The predicted Mg released within the first 10 years, enabled
639 minor quantities of calcite to transform into dolomite, whilst the Al and Si released con-
640 tributed to the formation of boehmite (Figure 10e,f). Muscovite reacted slowly, whereas
641 feldspars initially remained stable. However, K-feldspar was predicted to react after 100
642 years of simulated time, when chlorite was removed from the system. There was potential
643 for Fe hydro-oxides to be formed in the TS sample due to the relatively large amounts of
644 Fe released from ankerite breakdown (Figure 10e,f). K gradually replaced Ca in the ex-
645 changeable sites (Figure 10g, h).

646

Insert Figure 8

647

648 Numerous previous experimental and modelling studies have concluded that car-
649 bonates are the first phases to react upon addition of CO₂, and saturation is quickly at-
650 tained. Incongruent hydrolysis of aluminosilicates then becomes the main rate-limiting
651 reaction. Moreover, the aluminosilicate:carbonate ratio should be initially larger in order
652 to maintain long-term acid consumption capacity (Allan et al., 2011). In our case, chlorite

653 (and in a lesser extend muscovite) is the main consumer of the generated acid.
 654 Phyllosilicates exhibit high surface area and are susceptible to alteration. Their incongru-
 655 ent dissolution provides divalent cations, especially K and Mg, which promotes the pre-
 656 cipitation of secondary phases. This is in accordance with observations made by Carroll
 657 et al. (2013) who found that phyllosilicate hydrolysis is the rate-limiting reaction, when
 658 micas are present. Moreover, a sandstone experiment conducted for 1.5 years (P=10MPa,
 659 T=40°C, NaCl 20%) by Rathnaweera et al. (2016) showed dissolution of calcite, siderite
 660 and quartz.

661 The predicted geochemical reactions were compared to paragenetic sequences
 662 observed in sandstones from existing oil and gas fields. In the Werkendam gas field
 663 (Netherlands), the mineralogical assemblage consists of kaolinite which reacted with K-
 664 feldspar to form illite and quartz, whereas dolomite and siderite are the main carbonates
 665 (Koenen et al., 2013). CO₂ has been accumulating in Montmiral Triassic Sandstone since
 666 15 Ma ago, leading to the formation of kaolinite at the expense of K-feldspar, corrosion
 667 of ankerite and precipitation of barite, and ankerite/dolomite phases as secondary prod-
 668 ucts. Dawsonite was not observed (Czernichowski-Lauriol et al., 2006). The simulated
 669 geochemical sequences were in accordance with observations from UK oilfields, where
 670 carbonates and feldspars are not equilibrated with the current CO₂ of the reservoir
 671 (Haszeldine et al., 2005).

672

673 **3.4. Sensitivity tests and model limitations**

674 The proposed model partially reproduced the experimental data. The kinetic models pre-
 675 dicted the broad trend of the reactions, but failed to reproduce the exact amount of react-
 676 ing phases (quantitative mineralogical analysis of the solids after reaction with CO₂ gave
 677 values lower than those calculated by the models. Moreover, the calculated aluminium
 678 contents were much higher than those analysed in the sampled fluids. These discrepancies
 679 could be minimized by taking into account some identified uncertainties:

- 680 - Firstly, the model used the chemistry and thermodynamic data of ideal mineral phas-
 681 es. However, some phase involved may not be pure. So, for example, it is possible
 682 that chlorite and calcite could contain some iron, explaining its concentration in the
 683 analyzed fluids.
- 684 - Secondly, ion exchange capacity and surface areas were not measured, but approxi-
 685 mated by the mineral content and grain size. In order to simplify calculations, these
 686 values remained constant, although both mineral mass and size were changed during
 687 the dissolution/precipitation reactions.
- 688 - Lastly, the reactive fraction λ was a fitting parameter in order for the model to match
 689 the experimental data. As we lack a more detailed series of experiments to determine
 690 the actual solid fraction that reacted with the brine, this parameter would add to the
 691 uncertainty of the proposed models.

692

693 The role of the above uncertainties on the viability of the model results was evaluated by
694 running sensitivity tests considering the cation exchange capacity, the reactive surface
695 areas, and formation of possible precipitates.

696 **3.4.1. Effect of cation exchange capacity**

697 Cation exchange capacity was used mainly to simulate the initial fast increase of Ca, Mg
698 and HCO_3^- during the reaction of the solids with the N_2 -saturated brine. The importance
699 of cation exchange was represented using CEC values from zero to a maximum according
700 to the mineralogy of the samples. All other parameters remained unchanged.

701 The concentrations of Ca, Mg and HCO_3^- were the most affected by the different
702 CEC values tested, and thus the amounts of the minerals involved. The use of CEC value
703 affected mainly the reaction behavior of carbonates, the incongruent dissolution of K-
704 feldspar and chlorite, and formation of boehmite and silica (Figure 11). Calcite and chlo-
705 rite were dissolved and the released magnesium enabled the precipitation of dolomite.
706 The maximum amount of dolomite was achieved when no CEC was used, whereas more
707 calcite was dissolved at the highest CEC value. However, predicted steady-state was
708 reached after 100 years. On the other hand, chlorite and K-feldspar dissolved, releasing
709 silica regardless of the tested exchange capacity. It was concluded that cation exchange
710 was an important process occurring during equilibrium, which was overwhelmed by the
711 kinetically induced reactions between the solids and the dissolved CO_2 .

712

Insert Figure 11

713

714 **3.4.2. Effect of reactive surface area**

715 The determination of reactive surface area is a rather difficult task. Even if a surface area
716 value had been measured (i.e. by BET measurements), its reactivity depends on the
717 anomalies and dislocations on the surface of the grains. If λ is equal to 1, the whole grain
718 is reacting with the solution, and reaction rate is maximized. The lower the λ value, the
719 more that reactivity is minimized. Sensitivity test was run using λ values from 0.00001
720 (practically smooth surface) to 1 (a rough surface) (Figure 12, 13).

721 The main reactive phases in the PS sample were the carbonates, muscovite, chlo-
722 rite and quartz. The amounts of feldspar dissolution and clay precipitation were less than
723 $1\mu\text{mol}$, and so they were omitted from the figures. When a smooth surface was used (Fig-
724 ure 12a,b & 13a,b), the rate-limiting reaction was aluminosilicate dissolution, which oc-
725 curred after 10 years, along with a change in the carbonate phases. When λ was increased
726 by two orders of magnitude, carbonate transformation was brought forward up by approx-
727 imately 5 years, and chlorite hydrolysis prevailed (Figure 12c, d & 13c, d). For simula-

728 tions with a fully reactive surface area (Figure 12e, f & 13e, f), chlorite was completely
729 dissolved within 100 years, and K-feldspar hydrolysis became the rate-limiting step. The
730 predicted excessive Mg content during the first 100 years promoted dolomite precipita-
731 tion over calcite in the PS simulation. None of the simulations predicted the formation of
732 dawsonite, magnesite or siderite.

733 *Insert Figure 12*

734 *Insert Figure 13*

735

736 **3.4.3. Effect of secondary precipitates**

737 In the proposed model the fluid was equilibrated with boehmite to counterbalance
738 the high Al content extracted from the simulations. Most of the other selected secondary
739 phases (i.e. magnetite, siderite, gibbsite, illite, etc) did not kinetically form under the sim-
740 ulated conditions (perhaps the kinetic data used do not represent the occurring reaction
741 rates). The importance of these phases in the evolution of the primary mineralogy of the
742 samples was assessed via a semi-kinetic model, where kinetic reactions were used for the
743 primary phases with CO₂-saturated brine and equilibrium reactions for all the secondary
744 precipitates.

745 The CO₂-brine-rock system was equilibrated with boehmite (SI=0). The other
746 secondary phases were either allowed or forced to attain equilibrium. In the first case,
747 dawsonite, gibbsite, magnesite, illite, goethite, and Fe(OH)₃ freely reacted (dis-
748 solved/precipitated) until SI=0 (Figure 14a-d). Under these assumptions, dawsonite was
749 formed instantaneously (consuming the Al required for boehmite growth), though the ki-
750 netic model did not predict its formation. This was also the case in simulations conducted
751 by Hellevang et al. (2013). In the second case, the aforementioned phases were forced to
752 reach the over- or undersaturation using the indices calculated in Session 3.4.1. This re-
753 sulted in the formation of gibbsite as the main precipitate (Figure 14e-h). Illite and
754 boehmite were predicted to form at the very start of all simulations, during the first dec-
755 ade. Siderite growth resulted from ankerite dissolution after 1000 years of simulated reac-
756 tions.

757 In either case, the overall mass transfer as discussed in the base case scenario of
758 Section 3.3.4 and presented in detail in Figure 11 (diagrams e & f), shows that the semi-
759 kinetic approach does not affect the kinetic reactions of the primary phases. However, it
760 fails to predict accurately the formation of the secondary phases, as some of them are fa-
761 voured and expected under equilibrium conditions. Thus, the kinetic modelling approach
762 would be more realistic if it is important to describe in detail the mineral phases that help
763 CO₂ trapping. However, if the main concern is the overall mineralogical evolution of the

764 reservoir, the use of a semi-kinetic (i.e. equilibrium and kinetic) model would provide
765 adequate levels of detail.

766

767 *Insert Figure 14*

768

769 **Conclusions**

770 Representative sandstone samples from Mesohellenic Trough (NW Greece) were tested
771 to investigate the geochemical reactions that occur when they come in contact with CO₂-
772 saturated brine (~0.5M) under representative in-situ conditions. A PHREEQC-based geo-
773 chemical model was used, and for shorter timescales was calibrated using mineralogical
774 and chemical results from lab experiments.

775 Geochemical reactions that occurred within the sandstone-brine-CO₂ system were
776 limited and the absence of noticeable changes in the sandstone samples indicated that the
777 proposed reactions proceeded very slowly, but included (a) mass transfer among car-
778 bonate phases, and (b) the incongruent dissolution of phyllosilicates. No secondary car-
779 bonates were observed at the end of the experiments. However, simulation results for a 10
780 ka time period predicted that chlorite was expected to dissolve completely within 100
781 years, leading to boehmite growth and increasing the mass of dolomite. Feldspars were
782 expected to react at a later stage in the reaction sequence.

783 A number of key uncertainties were identified, such as reactive surface area, cation
784 exchange capacity, and secondary mineral growth. The impact of these on the simula-
785 tions was assessed using sensitivity tests, and these showed that the silicate hydrolysis is
786 the rate-limiting reaction on the system. Furthermore, the growth of secondary precipi-
787 tates was favored under local equilibrium conditions.

788 The geochemical experiments and modelling lend support to the view that Penta-
789 lofos and Tsotyli sandstone formations of the Mesohellenic Trough are suitable for the
790 long-term storage of CO₂ produced in the neighbouring lignite-fired power plants, at least
791 in terms of mineralogy and geochemistry. Continued optimization of the model used,
792 combined with more information on the structural properties of sandstone formations of a
793 sedimentary basin such as the Mesohellenic Trough (porosity, permeability, etc.), could
794 help in their further evaluation as a potential storage structure for CO₂.

795

796

797 **Acknowledgments**

798 This research has been co-financed by the European Union (European Social Fund –
 799 ESF) and Greek national funds through the Operational Program "Education and Lifelong
 800 Learning" of the National Strategic Reference Framework (NSRF) - Research Funding
 801 Program: Thales. Investing in knowledge society through the European Social Fund. The
 802 authors would also specifically like to thank all the staff of the British Geological Survey
 803 (BGS) that were involved in the batch experiments on samples of Greek sandstones, and
 804 that contributed to the sample preparation and provided the fluid analysis results. The
 805 staff of the National and Kapodistrian University of Athens and Dr. Ioannis Baziotis from
 806 the Agricultural University of Athens are thanked for supporting this work. Special
 807 thanks should also be given to Alexandros Tasianas and Petros Koutsovitis from CERTH
 808 for their contribution in redacting this paper. GP and CR publish with the permission of
 809 the Executive Director of the British Geological Survey, NERC.

810

811 **Appendix A. Supplementary data**

812

813 **REFERENCES**

- 814 Alemu, B.L., Aagaard, P., Munz, I.A., Skurtveit, E., 2011. Caprock interaction with CO₂:
 815 A laboratory study of reactivity of shale with supercritical CO₂ and brine. *Appl.*
 816 *Geochemistry* 26, 1975–1989. doi:10.1016/j.apgeochem.2011.06.028
- 817 Allan, M.M., Turner, A., Yardley, B.W.D., 2011. Relation between the dissolution rates
 818 of single minerals and reservoir rocks in acidified pore waters. *Appl. Geochemistry*
 819 26, 1289–1301. doi:10.1016/j.apgeochem.2011.05.002
- 820 Appelo, C.A., Postma, D., 2005. *Geochemistry, groundwater and pollution*, Fifth. ed.
 821 CRC Press, Amsterdam, Netherlands.
- 822 Baraka, A., 2015. Investigation of temperature effect on surface-interaction and diffusion
 823 of aqueous-solution/porous-solid adsorption systems using diffusion-binding model.
 824 *J. Environ. Chem. Eng.* 3, 129–139. doi:10.1016/j.jece.2014.11.001
- 825 Bateman, K., Turner, G., Pearce, J.M., Noy, D.J., Birchall, D., Rochelle, C.A., 2005.
 826 Large-scale column experiment: Study of CO₂, porewater, rock reactions and model
 827 test case. *Oil Gas Sci. Technol.* doi:10.2516/ogst:2005010
- 828 Black, J.R., Carroll, S.A., Haese, R.R., 2014. Rates of mineral dissolution under CO₂
 829 storage conditions. *Chem. Geol.* 399, 134–144. doi:10.1016/j.chemgeo.2014.09.020
- 830 Brunn, J., 1956. Contribution a l' étude géologique du Pinde serpenrional et d' une partie
 831 de la Macedoine occidentale. *Ann. Géologique des Pays Hellénique*, Vol. 7.
- 832 Carroll, S., McNab, W., Dai, Z., Torres, S., 2013. Reactivity of Mt. Simon sandstone and

- 833 the Eau Claire shale under CO₂ storage conditions. *Environ. Sci. Technol.*
- 834 Czernichowski-Lauriol, I., Rochelle, C., Gaus, I., Azaroual, M., Pearce, J., Durst, P.,
835 2006. Geochemical Interactions between CO₂, Pore-Waters and Reservoir Rocks.
836 *Adv. Geol. Storage Carbon Dioxide - Int. Approaches to Reduce Anthropog.*
837 *Greenh. Gas Emiss. Nato Sci. Ser. IV, Vol. 65* 65, 157–174. doi:10.1007/1-4020-
838 4471-2_14
- 839 De Silva, G.P.D., Ranjith, P.G., Perera, M.S.A., 2015. Geochemical aspects of CO₂
840 sequestration in deep saline aquifers: A review. *Fuel* 155, 128–143.
841 doi:10.1016/j.fuel.2015.03.045
- 842 Delany, J.M., Lundeen, S.R., 1991. The LLNL thermochemical data base--revised data
843 and file format for the EQ3/6 package. Lawrence Livermore National Laboratory.
- 844 Duan, Z., Moller, N., Weare, J.H., 1995. Equation of State for the NaCl-H₂O-CO₂ System
845 - Prediction of Phase-Equilibria and Volumetric Properties. *Geochim. Cosmochim.*
846 *Acta* 59, 2869–2882.
- 847 Duan, Z., Sun, R., 2003. An improved model calculating CO₂ solubility in pure water and
848 aqueous NaCl solutions from 273 to 533 K and from 0 to 2000 bar. *Chem. Geol.*
849 193, 257–271. doi:10.1016/S0009-2541(02)00263-2
- 850 Fischer, S., Zemke, K., Liebscher, A., Wandrey, M., 2011. Petrophysical and
851 petrochemical effects of long-term CO₂- exposure experiments on brine-saturated
852 reservoir sandstone. *Energy Procedia* 4, 4487–4494.
853 doi:10.1016/j.egypro.2011.02.404
- 854 Galarza, C., Buil, B., Peña, J., Martín, P.L., Gómez, P., Garralón, a., 2013. Preliminary
855 Results from the Experimental Study of CO₂-Brine-Rock Interactions at Elevated T
856 & P: Implications for the Pilot Plant for CO₂ Storage in Spain. *Procedia Earth*
857 *Planet. Sci.* 7, 272–275. doi:10.1016/j.proeps.2013.03.097
- 858 García-Rios, M., Luquot, L., Soler, J.M., Cama, J., 2013. Laboratory-Scale Interaction
859 between CO₂-Rich Brine and Reservoir Rocks (Limestone and Sandstone). *Procedia*
860 *Earth Planet. Sci.* 7, 109–112. doi:10.1016/j.proeps.2013.03.013
- 861 Gaus, I., 2010. Role and impact of CO₂-rock interactions during CO₂ storage in
862 sedimentary rocks. *Int. J. Greenh. Gas Control* 4, 73–89.
863 doi:10.1016/j.ijggc.2009.09.015
- 864 Gaus, I., Le Guern, C.C., Pearce, J., Pauwels, H.H., Shepherd, T., Hatziyannis, G.,
865 Metaxas, A., Hatziyannis, G., Metaxas, A., 2005. Comparison of long-term
866 geochemical interactions at two natural CO₂-analogues: Montmiral (Southeast
867 Basin, France) and Messokampos (Florina Basin, Greece) case studies, in:
868 *Proceedings of the 7th International Conference on Greenhouse Gas Control*
869 *Technologies* 5– September 2004, Vancouver, Canada. pp. 561–569.
870 doi:10.1016/B978-008044704-9/50057-4
- 871 Gunter, W.D., Perkins, E.H., McCann, T.J., 1993. Aquifer disposal of CO₂-rich gases:

- 872 Reaction design for added capacity. *Energy Convers. Manag.* doi:10.1016/0196-
873 8904(93)90040-H
- 874 Gunter, W.D., Wiwehar, B., Perkins, E.H., 1997. Aquifer disposal of CO₂-rich
875 greenhouse gases: Extension of the time scale of experiment for CO₂-sequestering
876 reactions by geochemical modelling. *Mineral. Petrol.* doi:10.1007/BF01163065
- 877 Haszeldine, R.S., Quinn, O., England, G., Wilkinson, M., Shipton, Z.K., Evans, J.P.,
878 Heath, J., Crossey, L., Ballentine, C.J., Graham, C.M., 2005. Natural geochemical
879 analogues for carbon dioxide storage in deep geological porous reservoirs, a United
880 Kingdom perspective. *Oil Gas Sci. Technol.* 60, 33–49. doi:10.2516/ogst:2005004
- 881 Hellevang, H., Declercq, J., Aagaard, P., 2011. Why is Dawsonite Absent in CO₂
882 Charged Reservoirs? *Oil Gas Sci. Technol. – Rev. d'IFP Energies Nouv.*
883 doi:10.2516/ogst/2011002
- 884 Hellevang, H., Pham, V.T., Aagaard, P., 2013. Kinetic modelling of CO₂-water-rock
885 interactions. *Int. J. Greenh. Gas Control* 15, 3–15. doi:10.1016/j.ijggc.2013.01.027
- 886 Horner, K.N., Schacht, U., Haese, R.R., 2015. Characterizing long-term CO₂-water-rock
887 reaction pathways to identify tracers of CO₂ migration during geological storage in a
888 low-salinity, siliciclastic reservoir system. *Chem. Geol.* 399, 123–133.
889 doi:10.1016/j.chemgeo.2014.09.021
- 890 Huq, F., Blum, P., Marks, M.A.W., Nowak, M., Haderlein, S.B., Grathwohl, P., 2012.
891 Chemical changes in fluid composition due to CO₂ injection in the Altmark gas
892 field: Preliminary results from batch experiments. *Environ. Earth Sci.* 67, 385–394.
893 doi:10.1007/s12665-012-1687-y
- 894 Huq, F., Haderlein, S.B., Cirpka, O.A., Nowak, M., Blum, P., Grathwohl, P., 2015. Flow-
895 through experiments on water-rock interactions in a sandstone caused by
896 CO₂ injection at pressures and temperatures mimicking reservoir
897 conditions. *Appl. Geochemistry* 58, 136–146.
898 doi:10.1016/j.apgeochem.2015.04.006
- 899 Johnson, J.W., Nitao, J., Knauss, K.G., 2004. Reactive Transport Modelling of CO₂
900 Storage in Saline Aquifers to Elucidate Fundamental Processes, Trapping
901 Mechanisms, and Sequestration Partitioning. *Geol. Soc. London Spec. Publ.* 233,
902 107–128.
- 903 Kampman, N., Bickle, M., Wigley, M., Dubacq, B., 2014. Fluid flow and CO₂-fluid-
904 mineral interactions during CO₂-storage in sedimentary basins. *Chem. Geol.* 369,
905 22–50. doi:10.1016/j.chemgeo.2013.11.012
- 906 Kaszuba, J.P., Janecky, D.R., Snow, M.G., 2003. Carbon dioxide reaction processes in a
907 model brine aquifer at 200°C and 200 bars: Implications for geologic sequestration
908 of carbon. *Appl. Geochemistry* 18, 1065–1080. doi:10.1016/S0883-2927(02)00239-
909 1
- 910 Kaszuba, J.P., Yardley, B.W.D., Andreani, M., 2013. Experimental Perspectives of

- 911 Mineral Dissolution and Precipitation due to Carbon Dioxide-Water-Rock
912 Interactions. *Rev. Mineral. Geochemistry* 77, 153–188.
- 913 Koenen, M., Wasch, L.J., Van Zalinge, M.E., Nelskamp, S., 2013. Werkendam, the
914 Dutch Natural Analogue for CO₂ Storage – Long-term Mineral Reactions. *Energy*
915 *Procedia* 37, 3452–3460. doi:10.1016/j.egypro.2013.06.235
- 916 Koukoulas, N., Ziogou, F., Gemeni, V., 2009. International Journal of Greenhouse Gas
917 Control Preliminary assessment of CO₂ geological storage opportunities in Greece
918 3, 502–513. doi:10.1016/j.ijggc.2008.10.005
- 919 Lasaga, A.C., 1984. Chemical kinetics of water-rock interactions. *J. Geophys. Res.* 89,
920 4009–4025.
- 921 Lin, H., Fujii, T., Takisawa, R., Takahashi, T., Hashida, T., Fujii, A.T., Takisawa, A.R.,
922 2008. Experimental evaluation of interactions in supercritical CO₂/water/rock
923 minerals system under geologic CO₂ sequestration conditions. *J. Mater. Sci.* 43,
924 2307–2315. doi:10.1007/s10853-007-2029-4
- 925 Lu, P., Fu, Q., Seyfried, W.E., Hedges, S.W., Soong, Y., Jones, K., Zhu, C., 2013.
926 Coupled alkali feldspar dissolution and secondary mineral precipitation in batch
927 systems - 2: New experiments with supercritical CO₂ and implications for carbon
928 sequestration. *Appl. Geochemistry* 30, 75–90.
929 doi:10.1016/j.apgeochem.2012.04.005
- 930 Luquot, L., Andreani, M., Gouze, P., Camps, P., 2012. CO₂ percolation experiment
931 through chlorite/zeolite-rich sandstone (Pretty Hill Formation - Otway Basin-
932 Australia). *Chem. Geol.* 294–295, 75–88. doi:10.1016/j.chemgeo.2011.11.018
- 933 Marty, N.C.M., Claret, F., Lassin, A., Tremosa, J., Blanc, P., Made, B., Giffaut, E.,
934 Cochepin, B., Tournassat, C., 2015. A database of dissolution and precipitation rates
935 for clay-rocks minerals. *Appl. Geochemistry* 55, 108–118.
936 doi:10.1016/j.apgeochem.2014.10.012
- 937 Mohd Amin, S., Weiss, D.J., Blunt, M.J., 2014. Reactive transport modelling of geologic
938 CO₂ sequestration in saline aquifers: The influence of pure CO₂ and of mixtures of
939 CO₂ with CH₄ on the sealing capacity of cap rock at 37°C and 100bar. *Chem. Geol.*
940 367, 39–50. doi:10.1016/j.chemgeo.2014.01.002
- 941 Palandri, J.L., Kharaka, Y.K., 2004. A compilation of rate parameters of water-mineral
942 interaction kinetics for application to geochemical modeling. *U.S. Geol. Surv. Open*
943 *file Rep.* 2004–1068, 71. doi:10.1098/rspb.2004.2754
- 944 Parkhurst, D., Appelo, C., 1999. User's guide to PHREEQC (Version 2) - A computer
945 program for speciation, batch-reaction, one-dimensional transport, and inverse
946 geochemical calculations.
- 947 Rathnaweera, T.D., Ranjith, P.G., Perera, M.S.A., 2016. Experimental investigation of
948 geochemical and mineralogical effects of CO₂ sequestration on flow characteristics
949 of reservoir rock in deep saline aquifers. *Sci. Rep.* 6, 19362. doi:10.1038/srep19362

- 950 Schoonen, M.A.A., Sklute, E.C., Dyar, M.D., Strongin, D.R., 2012. Reactivity of
951 sandstones under conditions relevant to geosequestration: 1. Hematite-bearing
952 sandstone exposed to supercritical carbon dioxide commingled with aqueous sulite
953 or sulfide solutions. *Chem. Geol.* doi:10.1016/j.chemgeo.2011.11.013
- 954 Smyth, J.R., McCormick, T.C., 1995. Crystallographic data for minerals. *Miner. Phys.*
955 *Crystallogr. A Handb. Phys. Constants* 2, 1–17. doi:10.1029/RF002p0001
- 956 Sorensen, J.A., Holubnyak, Y.I., Hawthorne, S.B., Miller, D.J., Eylands, K., Steadman,
957 E.N., Harju, J.A., 2009. Laboratory and numerical modeling of geochemical
958 reactions in a reservoir used for CO₂ storage. *Energy Procedia* 1, 3391–3398.
959 doi:10.1016/j.egypro.2009.02.128
- 960 Tester, J.W., Worley, W.G., Robinson, B.A., Grigsby, C.O., Feerer, J.L., 1994.
961 Correlating quartz dissolution kinetics in pure water from 25 to 625°C. *Geochim.*
962 *Cosmochim. Acta* 58, 2407–2420. doi:10.1016/0016-7037(94)90020-5
- 963 Tremosa, J., Castillo, C., Vong, C.Q., Kervevan, C., Lassin, A., Audigane, P., 2014.
964 Long-term assessment of geochemical reactivity of CO₂ storage in highly saline
965 aquifers: Application to Ketzin, In Salah and Snohvit storage sites. *Int. J. Greenh.*
966 *Gas Control* 20, 2–26. doi:10.1016/j.ijggc.2013.10.022
- 967 Vamvaka, A., 2009. Geometry of deformation and kinematic analysis in Mesohellenic
968 Trough. Aristotle University of Thessaloniki.
- 969 Van Pham, T.H., Aagaard, P., Hellevang, H., 2012. On the potential for CO₂ mineral
970 storage in continental flood basalts – PHREEQC batch- and 1D diffusion–reaction
971 simulations. *Geochem. Trans.* 13, 5. doi:10.1186/1467-4866-13-5
- 972 Van Pham, T.H., Lu, P., Aagaard, P., Zhu, C., Hellevang, H., 2011. On the potential of
973 CO₂-water-rock interactions for CO₂ storage using a modified kinetic model. *Int. J.*
974 *Greenh. Gas Control* 5, 1002–1015. doi:10.1016/j.ijggc.2010.12.002
- 975 Wigand, M., Carey, J.W., Schütt, H., Spangenberg, E., Erzinger, J., 2008. Geochemical
976 effects of CO₂ sequestration in sandstones under simulated in situ conditions of deep
977 saline aquifers. *Appl. Geochemistry* 23, 2735–2745.
978 doi:10.1016/j.apgeochem.2008.06.006
- 979 Wilke, F.D.H., Vasquez, M., Wiersberg, T., Naumann, R., Erzinger, J., 2012. On the
980 interaction of pure and impure supercritical CO₂ with rock forming minerals in
981 saline aquifers: An experimental geochemical approach. *Appl. Geochemistry*.
982 doi:10.1016/j.apgeochem.2012.04.012
- 983 Wilson, M., Monea, M., 2005. IEA GHG Weyburn CO₂ monitoring and storage project
984 summary report 2000-2004. *Proc. 7th Int. Conf. Greenh. Gas Control Technol.*
985 (GHGT-7), Sept. 5-9.
- 986 Worden, R.H., 2006. Dawsonite cement in the Triassic Lam Formation, Shabwa Basin,
987 Yemen: A natural analogue for a potential mineral product of subsurface CO₂
988 storage for greenhouse gas reduction. *Mar. Pet. Geol.* 23, 61–77.

- 989 doi:10.1016/j.marpetgeo.2005.07.001
- 990 Yu, Z., Liu, L., Yang, S., Li, S., Yang, Y., 2012. An experimental study of CO₂-brine-
991 rock interaction at in situ pressure-temperature reservoir conditions. *Chem. Geol.*
992 326–327, 88–101. doi:10.1016/j.chemgeo.2012.07.030
- 993 Zelilidis, A., Piper, D., Kontopoulos, N., 2002. Sedimentation and basin evolution of the
994 Oligocene-Miocene Mesohellenic basin, Greece, in: *AAPG Bulletin*, 86(1). pp.
995 161–182.
- 996 Zhang, M., Pu, J., 2011. Mineral materials as feasible amendments to stabilize heavy
997 metals in polluted urban soils. *J. Environ. Sci.* 23, 607–615.
- 998 Zhou, B., Liu, L., Zhao, S., Ming, X.R., Oelkers, E.H., Yu, Z.C., Zhu, D.F., 2014.
999 Dawsonite formation in the beier sag, hailar basin, NE China tuff: A natural analog
1000 for mineral carbon storage. *Appl. Geochemistry* 48, 155–167.
1001 doi:10.1016/j.apgeochem.2014.07.015

1002

1003

LIST OF FIGURES

1004

1005 Figure 1: Geological map (a) and stratigraphic column (b) of Mesohellenic Trough (mod-
1006 ified after Brunn, 1956). Red and blue symbols on the map denote the sampling locations
1007 of the Tsotyli and Pentalofos sandstones respectively.

1008

1009 Figure 2: Experimental arrangement for the crushed sandstones samples.

1010

1011 Figure 3: Flow chart of the steps followed in constructing the geochemical models.

1012

1013 Figure 4: Light microscopy images of uncrushed TS and PS samples in thin section under
1014 parallel (A, B) and crossed (C, D) nicols. Qtz=quartz, Fsp=feldspars, Cal=calcite,
1015 Ms=moscovite, Bt=biotite, Ol=olivine, Op= Operculina sp.

1016

1017 Figure 5: SEM images of uncrushed TS and PS samples. Qtz=quartz, Fsp=feldspars,
1018 Cal=calcite, Mca=mica. Blue and yellow areas show the porosity and clay matrix, respec-
1019 tively.

1020

1021 Figure 6: XRD patterns of the TS and PS samples prior and after the sCO₂ injection.
1022 Qz=quartz, Or=orthoclase, Ab=albite, Cal=calcite, Kln=kaolinite, Dol=dolomite,
1023 Ms=muscovite, Ank=ankerite, Clc=clinochlore, Mnt=montmorillonite.

1024

1025 Figure 7: Modelled (lines) and experimental (symbols) chemical data of fluid samples as
1026 a function of time from the start (equilibrium reactions) to the end (kinetic reaction) of the
1027 experiment.

1028

1029 Figure 8: Saturation indices (SI) for the mineral phases of the sandstone samples.

1030

1031 Figure 9: Simulated mineral fractions of the primary (a,b), accessory (c,d) and possible
1032 secondary (e,f) mineral phases of the sandstone samples and cation distribution (g,h) as a
1033 function of the experimental time.

1034

1035 Figure 10: Predicted evolution of primary (a,b), accessory (c,d) and secondary (e,f) min-
1036 eral phases, and cation exchange reactions (g,h) for PS and TS samples over 10 ka.

1037

1038 Figure 11: Sensitivity of cation exchange capacity on the CO₂-brine-solid interactions for
1039 an estimated time of 10 ka. CEC values ranged from 0 (no exchange involved) to the
1040 maximum calculated value according to the composition of the samples.

1041

1042

1043 Figure 12: Sensitivity of reactive factor λ on the solid-CO₂ interactions for Pentalofos
1044 sample (PS) for a time period of 10 ka. Values varied from 10⁻⁵, denoting a smooth sur-
1045 face, to 1 corresponding to a fully reactive surface.

1046

1047 Figure 13: Sensitivity of reactive factor λ on the solid-CO₂ interactions for Tsotyli sample
1048 (TS) for a time period of 10 ka. Values varied from 10⁻⁵, denoting a smooth surface, to 1
1049 corresponding to a fully reactive surface.

1050

1051 Figure 14: Effect of the equilibrium of sandstone samples with respective secondary
1052 phases, on the geochemical reactions for a time period of 10 ka.

1053

1054

1055

Assessment of the impact of CO₂ storage in sandstone formations by experimental studies and geochemical modeling: the case of the Mesohellenic Trough, NW Greece

SUPPLEMENTARY CONTENT

APPENDIX A: REACTION RATES AND THERMODYNAMIC DATA

Reaction dissolution and precipitation rates were calculated using the Transition State Theory (TST) (Lasaga, 1984) (Eq. A1):

$$r_n = \pm k_n RS_A |1 - \Omega_n^p|^q \quad (\text{A1})$$

where k_n corresponds to the reaction rate constant ($\text{mol m}^{-2} \text{s}^{-1}$), RS_A to the reactive surface area ($\text{m}^2 \text{g}^{-1}$) and Ω_n to the saturation state and where p, q are constants. Positive and negative r_n values refer to dissolution and precipitation reactions respectively.

The reaction rate constant k_n depends on the reaction temperature and pH of the solution according to Arrhenius law (Eq. A2):

$$k_n = k_0^{\text{acid}} \exp \left[\frac{-E_a^{\text{acid}}}{R} \left(\frac{1}{T} - \frac{1}{298.15} \right) \right] + k_0^{\text{acid}} \exp \left[\frac{-E_a^{\text{acid}}}{R} \left(\frac{1}{T} - \frac{1}{298.15} \right) \right] a_{\text{H}}^{n(\text{acid})} + k_0^{\text{base}} \exp \left[\frac{-E_a^{\text{base}}}{R} \left(\frac{1}{T} - \frac{1}{298.15} \right) \right] a_{\text{OH}}^{n(\text{base})} \quad (\text{A2})$$

where k_0 is the intrinsic kinetic constant at 298K ($\text{in mol m}^{-2} \text{s}^{-1}$), R is the ideal gas constant ($8.314 \text{ J mol}^{-1} \text{ K}^{-1}$), T is the temperature (in K), E_a is the reaction activation energy (in kJ mol^{-1}), a is the ion activity and n is a constant. The acid part of the equation corresponds to the $[\text{H}^+]$ influence, whereas the base part to the $[\text{OH}^-]$, (or $[\text{HCO}_3^-]$ when carbonates are involved).

The saturation state Ω_n depends on the Gibbs free energy of the reaction (Eq. A3):

$$\Delta G_r = -RT \ln \Omega \quad (\text{A3})$$

The reactive surface area RS_A of a mineral corresponds to the fraction of the total surface area that is subject to dissolution or precipitation (Eq. A4).

$$RS_A = \lambda n MS_A \quad (\text{A4})$$

where n and M are the mineral moles and molar weight respectively, S_A is the specific surface area and λ the reactive fraction. The fraction λ equals to 1 when the whole surface area is reactive, and was estimated by the model. The surface area of a mineral is measured using BET methods, or calculated geometrically, using the relations (A5) and (A6):

$$S_A = \frac{6}{d_e p} \quad (\text{A5})$$

$$d_e = \frac{d_{\max} - d_{\min}}{\ln\left(\frac{d_{\max}}{d_{\min}}\right)} \quad (\text{A6})$$

where d_e , d_{\max} and d_{\min} are the effective, the maximum and the minimum particle diameter respectively and p the mineral density (Tester *et al.*, 1994).

In our study, the mineral moles n were calculated on the base of the wt% analysis of the samples. The effective diameter, d_e , of the solid particles and their reactive surface area, RS_A , were calculated for the 250-500 μm particle size, assuming a spherical shape of the grains.

The thermodynamic parameters of the selected minerals are presented in Table A.1. Most of them are included in Inl.dat database. Ankerite data were taken from Krupka *et al.* (2010). Moreover, some additional phases were selected to investigate their possible formation by the model. These phases include magnesite, siderite, dawsonite, boehmite, $\text{Fe}(\text{OH})_3$ and gibbsite. Kinetic dissolution and precipitation parameters are presented in Tables A.2 & A.3 (Palandri and Kharaka, 2004; Van Pham *et al.*, 2011; Marty *et al.*, 2015). As kinetic data for ankerite, dawsonite could not be identified in the literature, the respective parameters of another carbonate phase, dolomite, were taken as being similar, and were used instead. In the same manner, siderite data were used for magnesite, and boehmite for gibbsite and $\text{Fe}(\text{OH})_3$.

Table A.1: Thermodynamic data of the selected sandstone minerals at 25°C, used in the geochemical models (lInl.dat)

Mineral	Formula	Dissolution reaction	Log k_0 (25°C)	ΔH_r (kJ mol ⁻¹)
Albite	NaAlSi ₃ O ₈	NaAlSi ₃ O ₈ + 4H ⁺ = Al ³⁺ + Na ⁺ + 2H ₂ O + 3SiO ₂	2.76	-51.85
Orthoclase	KAlSi ₃ O ₈	KAlSi ₃ O ₈ + 4H ⁺ = Al ³⁺ + K ⁺ + 2H ₂ O + 3SiO ₂	-0.27	-23.94
Calcite	CaCO ₃	CaCO ₃ + H ⁺ = Ca ²⁺ + HCO ₃ ⁻	1.85	-25.71
Dolomite	CaMg(CO ₃) ₂	CaMg(CO ₃) ₂ + 2H ⁺ = Ca ²⁺ + Mg ²⁺ + 2HCO ₃ ⁻	2.51	-59.96
Montmorillonite	Na _{0.33} Mg _{0.33} Al _{1.67} Si ₄ O ₁₀ (OH) ₂	Na _{0.33} Mg _{0.33} Al _{1.67} Si ₄ O ₁₀ (OH) ₂ + 6H ⁺ = 0.33Mg ²⁺ + 0.33Na ⁺ + 1.67Al ³⁺ + 4H ₂ O + 4SiO ₂	2.48	-93.22
Kaolinite	Al ₂ Si ₂ O ₅ (OH) ₄	Al ₂ Si ₂ O ₅ (OH) ₄ + 6H ⁺ = 2Al ³⁺ + 2SiO ₂ + 5H ₂ O	6.81	-151.78
Muscovite	KAl ₃ Si ₃ O ₁₀ (OH) ₂	KAl ₃ Si ₃ O ₁₀ (OH) ₂ + 10H ⁺ = K ⁺ + 3Al ³⁺ + 3SiO ₂ + 6H ₂ O	13.59	-243.22
Clinochlore	Mg ₅ Al ₂ Si ₃ O ₁₀ (OH) ₈	Mg ₅ Al ₂ Si ₃ O ₁₀ (OH) ₈ + 16H ⁺ = 2Al ³⁺ + 3SiO ₂ + 5Mg ²⁺ + 12H ₂ O	67.24	-612.38
Quartz	SiO ₂	SiO ₂ = SiO ₂	-3.99	32.95
^aAnkerite	CaFe _{0.4} Mg _{0.6} (CO ₃) ₂	CaFe _{0.4} Mg _{0.6} (CO ₃) ₂ + 2H ⁺ = Ca ²⁺ + 0.4Fe ³⁺ + 0.6Mg ²⁺ + 2HCO ₃ ⁻	-19.59	-42.96
Dawsonite	NaAlCO ₃ (OH) ₂	NaAlCO ₃ (OH) ₂ + 3H ⁺ = Al ³⁺ + HCO ₃ ⁻ + Na ⁺ + 2H ₂ O	4.35	-76.35
Magnesite	MgCO ₃	MgCO ₃ + H ⁺ = HCO ₃ ⁻ + Mg ²⁺	2.29	-44.49
Siderite	FeCO ₃	FeCO ₃ + H ⁺ = Fe ²⁺ + HCO ₃ ⁻	-0.19	-32.53
Gibbsite	Al(OH) ₃	Al(OH) ₃ + 3H ⁺ = Al ³⁺ + 3H ₂ O	7.75	-102.79
Fe(OH)3	Fe(OH) ₃	Fe(OH) ₃ + 3H ⁺ = Fe ³⁺ + 3H ₂ O	5.65	-84.08
Goethite	FeOOH	FeOOH + 3H ⁺ = Fe ³⁺ + 2H ₂ O	0.53	-61.93
Boehmite	AlO ₂ H	AlO ₂ H + 3H ⁺ = Al ³⁺ + 2H ₂ O	7.56	-113.28

^a Thermodynamic data from (Van Pham, Aagaard and Hellevang, 2012)

Table A.2 : Dissolution kinetic parameters used in the geochemical models

Mineral	Acidic term		Neutral term		Base term		n (base)	p	q	Reference	
	k_0^{acid} (mol m ⁻² s ⁻¹)	E_a^{acid} (J mol ⁻¹)	$n^{(\text{acid})}$	k_0^{neu} (mol m ⁻² s ⁻¹)	E_a^{neu} (J mol ⁻¹)	k_0^{base} (mol m ⁻² s ⁻¹)					E_a^{base} (J mol ⁻¹)
Albite	8.50x10 ⁻¹¹	58000	0.34	5.10x10 ⁻²⁰	57000	1.40x10 ⁻¹⁰	56000	0.32	1.00	1.00	Marty et al. (2015)
Orthoclse	1.70x10 ⁻¹¹	31000	0.27	1.00x10 ⁻¹⁴	31000	1.40x10 ⁻¹⁰	31000	0.35	1.00	1.00	Marty et al. (2015)
^a Calcite	5.01x10 ⁻⁰¹	14400	1	1.55x10 ⁻⁰⁶	23500	3.30x10 ⁻⁰⁴	35400	1.00	1.00	1.00	Palandri & Kharaka (2004)
^b Dolomite	2.80x10 ⁻⁰⁴	46000	0.61	1.10x10 ⁻⁰⁸	31000	-	-	-	0.16	2.10	Marty et al. (2015)
Montmorillonite	5.30x10 ⁻¹¹	54000	0.69	9.30x10 ⁻¹⁵	63000	2.90x10 ⁻¹²	61000	0.34	0.17	10.34	Marty et al. (2015)
Kaolinite	7.50x10 ⁻¹²	43000	0.51	1.10x10 ⁻¹⁴	38000	2.50x10 ⁻¹¹	46000	0.58	1.00	1.00	Marty et al. (2015)
Muscovite	1.41x10 ⁻¹²	22000	0.37	2.82x10 ⁻¹⁴	22000	2.80x10 ⁻¹⁵	22000	-0.22	1.00	1.00	Palandri & Kharaka (2004)
Clinochlore	8.20x10 ⁻⁰⁹	17000	0.28	6.40x10 ⁻¹⁷	16000	6.90x10 ⁻⁰⁹	16000	0.34	1.00	1.00	Marty et al. (2015)
Quartz	-	-	-	6.40x10 ⁻¹⁴	77000	1.90x10 ⁻¹⁰	80000	0.34	1.00	1.00	Marty et al. (2015)
^b Ankerite	2.80x10 ⁻⁰⁴	46000	0.61	1.10x10 ⁻⁰⁸	31000	-	-	-	0.16	2.10	Marty et al. (2015)

^a Base term in respect to [HCO₃⁻]

^b Disordered (sedimentary) dolomite dissolution data were used.

Table A.3: Precipitation rate parameters

Precipitation Rates								
(Marty, et al., 2015)								
Mineral	Precipitation term		Additional term		n(add)	p	q	
	k_0^{pre} (mol m ⁻² s ⁻¹)	E_a^{pre} (J mol ⁻¹)	k_0^{add} (mol m ⁻² s ⁻¹)	E_a^{add} (J mol ⁻¹)				
Quartz	3.20x10 ⁻¹²	50000	-	-	-	4.58	0.54	
^a Calcite	1.80x10 ⁻⁰⁷	66000	1.90x10 ⁻⁰³	67000	1.63	0.5	2	
Dolomite	9.50x10 ⁻¹⁵	103000	-	-	-	1	1	
^b Ankerite	9.50x10 ⁻¹⁵	103000	-	-	-	1	1	
^b Dawsonite	9.50x10 ⁻¹⁵	103000	-	-	-	1	1	
^c Magnesite	1.60x10 ⁻¹¹	108000	-	-	-	1	1	
^d Montmorillonite	5.50x10 ⁻¹³	66000	-	-	-	0.06	1.68	
Kaolinite	5.50x10 ⁻¹³	66000	-	-	-	0.06	1.68	
^d Illite	5.50x10 ⁻¹³	66000	-	-	-	0.06	1.68	
Boehmite	-	-	3.1x10 ⁻⁰⁶	0	1	1	1	
^e Fe(OH) ₃	-	-	3.1x10 ⁻⁰⁶	0	1	1	1	
^e Gibbsite	-	-	3.1x10 ⁻⁰⁶	0	1	1	1	

^a Additional term in respect to [HCO₃⁻]

^b Dolomite precipitation data used for ankerite and dawsonite

^c Siderite precipitation parameters used for magnesite

^d Kaolinite precipitation data used for montmorillonite and illite

^e Boehmite precipitation data used for Fe(OH)₃ and gibbsite. Additional term in respect to [OH⁻]

APPENDIX B: Chemical analysis of the fluid samples

Table B.1: Fluid chemistry data for the batch experiment of Tsotyli Sandstone (TS) sample^a

Sampling date	Sample Code	pH at 20°C	Eh mV at 20°C	Ca mg L ⁻¹	Mg mg L ⁻¹	Na mg L ⁻¹	K mg L ⁻¹	HCO ₃ ⁻ mg L ⁻¹	Cl ⁻ mg L ⁻¹	Balance %	TIC (from alk) mg L ⁻¹	Si mg L ⁻¹	Al µg L ⁻¹
27/5/14	Brine	8.96	137.4	<10	<0.8	12940	1.2	ND	17230	7	0	<1.7	<18
5/6/14	1683/1	7.33	205.5	77	7.2	11898	5.3	97	17790	1	19	7	106
3/7/14	1683/2	7.51	109.4	84	9.5	11676	4.8	157	17546	1	31	8	23
7/7/14	1683/3	6.74	46.7	1140	41.7	12423	6.2	1119	17579	2	220	20	58
15/7/14	1683/4	6.73	6.4	1112	42.5	12159	6.2	1522	17100	1	300	22	50
22/7/14	1683/5	6.67	53.7	1211	46.8	12237	6.1	1404	18918	-3	276	24	58
28/7/14	1683/6	6.63	39.1	1018	49.1	12143	6.1	1494	17133	-1	294	25	<18
14/7/14	1683/7	6.66	33.7	1282	58.7	12421	6.4	1949	17271	-2	384	28	61
8/9/14	1683/8	6.79	52.1	1354	74.8	13388	6.8	1786	17766	2	352	34	48
20/10/14	1683/9	6.68	43.5	1258	83.2	12890	7.5	2154	17550	-2	424	36	36
25/11/14	1683/10	6.68	26.9	1195	102	12395	6.4	2714	18589	-9	534	40	48

Table B.1 (cont.)

Sampling date	Sample Code	Total Fe µg L ⁻¹	Oxidised Fe µg L ⁻¹	Reduced Fe µg L ⁻¹	Li µg L ⁻¹	Ti µg L ⁻¹	V µg L ⁻¹	Cr µg L ⁻¹	Co µg L ⁻¹	Ni µg L ⁻¹	Cu µg L ⁻¹	Ba µg L ⁻¹	Sr µg L ⁻¹	Mn µg L ⁻¹	Zn µg L ⁻¹
27/5/14	Brine	<42	<37.1	<4.9	<37	<0.6	<3	<1	<0.4	0.8	4.2	<5	9	<7	20
5/6/14	1683/1	<42	<42.3	0	86	<0.6	10	3	0.5	39	217	113	694	23	47
3/7/14	1683/2	1546	1325	221	65	<0.6	<3	<1	17.7	668	4.2	122	805	99	23
7/7/14	1683/3	1335	1157	178	69	<0.6	4	47	24.8	724	48.2	449	4094	1040	81
15/7/14	1683/4	3792	3270	522	70	1.4	4	10	23.6	715	38.7	450	4190	897	70
22/7/14	1683/5	579	505	75	71	1.1	4	5	24.9	624	65.1	481	4366	1004	100
28/7/14	1683/6	827	717	110	71	1.3	3	6	21	621	44.8	513	4215	576	47
14/7/14	1683/7	1274	1130	144	74	0.8	5	9	29.9	679	45.3	537	4602	1134	77
8/9/14	1683/8	1152	1061	91	77	0.8	6	5	34.3	724	59.5	543	4952	1111	61
20/10/14	1683/9	1101	996	105	84	<0.6	4	3	35.7	723	73.8	528	4834	1058	50
25/11/14	1683/10	1930	1802	128	96	1.1	4	2	37.1	696	20.0	567	4639	870	40

Table B.2: Fluid chemistry data for the batch experiment of Pentalofos Sandstone (PS) sample^a

Sampling Date	Sample Code	pH	Eh	Ca	Mg	Na	K	HCO ₃ ⁻	Cl ⁻	Balance	TIC (from alk)	Si	Al
		at 20°C	mVat 20°C	mg L ⁻¹	mg L ⁻¹	mg L ⁻¹	mg L ⁻¹	mg L ⁻¹	mg L ⁻¹	%	mg L ⁻¹	mg L ⁻¹	µg L ⁻¹
5/6/14	1684/1	7.31	187	114	11.3	13193	11.4	59	17685	7	12	7	64
3/7/14	1684/2	7.48	91.3	108	12.3	13538	12.3	90	16972	10	18	8	19
7/7/14	1684/3	6.74	-8.1	1136	40.5	12968	15.6	1152	17626	3	227	22	28
15/7/14	1684/4	6.67	27.8	1153	55.5	13258	18.4	1151	17461	5	227	33	19
22/7/14	1684/5	6.61	4.6	1145	68	13014	16.5	1492	17043	3	294	41	20
28/7/14	1684/6	6.49	39.1	1013	77.2	12832	16.5	1677	17411	0	330	47	<18
14/7/14	1684/7	6.76	9	1248	104	12616	16.4	1886	17555	-1	371	63	30
8/9/14	1684/8	6.78	32.7	1202	142	13030	17.3	1770	17088	2	348	78	<18
20/10/14	1684/9	6.71	22.1	1180	170	12574	16.7	1977	17325	-1	389	87	21
25/11/14	1684/10	6.71	13.6	1052	223	11943	15.4	2894	18758	-12	570	108	<18

Table B.2 (cont.)

Sampling date	Sample Code	Total Fe	Oxidised Fe	Reduced Fe	Li	Ti	V	Cr	Co	Ni	Cu	Ba	Sr	Mn	Zn
		µg L ⁻¹	µg L ⁻¹	µg L ⁻¹	µg L ⁻¹	µg L ⁻¹	µg L ⁻¹	µg L ⁻¹	µg L ⁻¹	µg L ⁻¹	µg L ⁻¹	µg L ⁻¹	µg L ⁻¹	µg L ⁻¹	µg L ⁻¹
5/6/14	1684/1	85	81	4	48	<0.6	45	2	0.6	31.2	1155	81	174	42	50
3/7/14	1684/2	3344	2934	410	46	<0.6	<3	<1	3.8	147	23.7	53	200	115	23
7/7/14	1684/3	7111	6199	912	54	<0.6	4	13	52.4	1185	120	186	863	1904	73
15/7/14	1684/4	2136	1863	273	65	0.8	4	11	57.6	1227	172	213	950	1490	75
22/7/14	1684/5	5334	4653	681	60	0.8	4	10	64.2	1361	217	204	956	1441	68
28/7/14	1684/6	2273	1976	298	59	<0.6	4	7	53.7	1276	199	219	940	961	93
14/7/14	1684/7	2949	2646	303	70	<0.6	7	6	82.1	1458	131	221	932	2289	68
8/9/14	1684/8	2606	2379	227	75	0.8	4	9	88.7	1540	198	231	943	1891	39
20/10/14	1684/9	2062	1846	216	72	<0.6	5	4	93.5	1543	77.5	218	926	2033	41
25/11/14	1684/10				88	1.1	5	6	83.9	1397	3.0	233	879	1058	43

NO₂⁻, NO₃⁻, HPO₄⁻², Br⁻, SO₄⁻² were below the detection limit